Advances in Nano Research, *Vol. 19, No. 5 (2025) 453-463*
https://doi.org/10.12989/anr.2025.19.5.453

Enhancing structural integrity of concrete skew panels with nanocomposite reinforcement

Fangbao Li[1], Yinghao Zhao*[2], Bashar Tarawneh[3,4], Mohammed A. El-Meligy[5] and Mohamed Sharaf[6]

[1]*Guangzhou Metro Design & Research Institute Co., Ltd. Guangzhou 510000, China*
[2]*School of Future Transportation, Guangzhou Maritime University, Guangzhou 510725, China*
[3]*Hourani Center for Applied Scientific Research, Al-Ahliyya Amman University, Amman, Jordan*
[4]*Faculty of Engineering, University of Jordan, Amman, Jordan*
[5]*Advanced Manufacturing Institute, King Saud University, P.O. Box 800, 11421, Riyadh, Saudi Arabia*
[6]*Department of Industrial Engineering, College of Engineering, King Saud University, Riyadh 12372, Saudi Arabia*

(*Received February 18, 2025, Revised October 8, 2025, Accepted October 13, 2025*)

Abstract. The structural performance of concrete skew panels is a vital parameter in civil engineering, especially in complex loading conditions. In this paper, a new approach is presented to improve the performance of skew cylindrical concrete panels by the use of nanocomposite reinforcement. In particular, the study evaluates functionally graded graphene oxide reinforced concrete (FG-GOPRC) as the reinforcement option of skew panels, utilizing this nanocomposite's mechanical properties under a variety of loading cases. The reinforcement will take on the Halpin-Tsai homogenization method of modelling to provide an accurate prediction of effective properties of the composite based on volume fraction and geometrical configuration of the nanomaterial in the concrete matrix. In order to derive the governing equations for both the bending and vibration analysis of the skew panels, a variational version of Hamilton's principle alongside the first order shear deformation theory (FSDT) is utilized. The Chebyshev-type Ritz technique is then employed to simply, yet accurately solve the governing equations. This allows for a comprehensive investigation on the influences of nanocomposite reinforcement on the concrete skew panels vibration characteristics. The results indicate that the FG-GOPRC nanocomposites produce a substantial increase in load capacity and durability when compared to conventional reinforcement types. These results have implications in the design and optimization of concrete panels for engineering purposes, especially when dealing with critical infrastructure under dynamic and static loading conditions. This study advances the field of nanoresearch in structural engineering, and suggests an effective and efficient method for concrete skew panels.

Keywords: Chebyshev-type Ritz method; concrete skew panels; Halpin-Tsai method; nanocomposite reinforcement; vibration characteristics

1. Introduction

Nanocomposite materials are revolutionizing engineering design, particularly in the field of structural reinforcement (Anh *et al*. 2021, Belabed *et al*. 2024, Tounsi *et al*. 2024). These materials combine the advantages of conventional composites with the superior properties of nanomaterials, such as nanoparticles, nanofibers, and nanotubes, to enhance the performance and longevity of structural components (Babaei *et al*. 2024). In concrete reinforcement, the integration of nanocomposites improves not only mechanical strength but also durability, offering better resistance to environmental factors like moisture, temperature variations, and chemical attacks (Ebrahimi and Ezzati, 2024). This is critical as infrastructure is often exposed to harsh conditions, which can lead to premature deterioration (Lu *et al*. 2025). The introduction of nanomaterials into composite systems offers remarkable improvements in the material's mechanical properties, such as increased tensile strength, enhanced stiffness, and superior fracture toughness (Li and Liu, 2025). Nanocomposite reinforcement enables the development of functionally graded materials, where the material properties gradually change across the structure, optimizing the performance in specific regions of the component (Arshid *et al*. 2025). This is particularly useful in applications like skew panels, beams, and slabs that experience varying stresses across their spans (Zhang *et al*. 2024). Incorporating nanocomposites into engineering design also leads to weight reductions while maintaining, or even improving, the material's load-bearing capacity (Mamidi *et al*. 2025). This is an important factor in reducing the overall environmental footprint of infrastructure, as it lowers material consumption and energy requirements during construction (Gayatri *et al*. 2024). Additionally, nanocomposite reinforcement has been shown to enhance the fatigue and impact resistance of structural elements, extending their service life and reducing maintenance costs (Liu *et al*. 2024). The versatility of nanocomposite materials makes them suitable for a wide range of engineering applications, from bridges and high-rise buildings to seismic-resistant structures (Afolabi and Ndou, 2024). Their ability to function at the nanoscale also opens up possibilities

*Corresponding author, Ph.D.,
E-mail: zhaoyinghao@gzmtu.edu.cn

ISSN: 2287-237X (Print), 2287-2388 (Online)

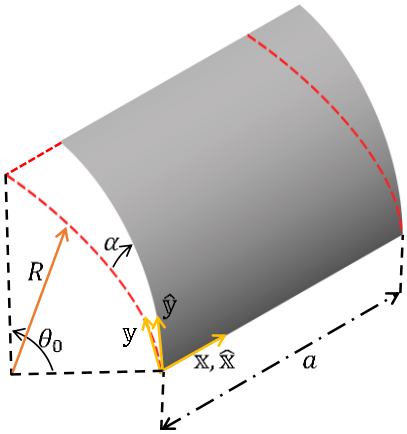

Fig. 1 Descriptions of skewed cylindrical panels using geometry

Table 1 Material properties of the system (Zhang *et al*. 2020)

Concrete (matrix)	GOPs
$v_m = 0.2$	$v_{GOP} = 0.165$
$\rho_m\ (\frac{kg}{m^3}) = 2300$	$\rho_{GOP}\ (\frac{kg}{m^3}) = 1090$
$E_m\ (Gpa) = 25$	$E_{GOP}\ (Gpa) = 444.8$
	$d_{GOP}(nm) = 500$
	$t_{GOP}(nm) = 0.95$

for self-healing and self-sensing materials, further advancing the capabilities of modern engineering systems (Rayhan *et al*. 2024). Moreover, as nanotechnology continues to evolve, the potential for more cost-effective and efficient production methods for nanocomposite materials offers exciting prospects for widespread adoption in structural engineering (Allahkarami and Tohidi, 2021). In this context, the role of nanocomposite reinforcement is crucial for the future of sustainable, resilient, and high-performance infrastructure design (Birenboim *et al*. 2019).

Stability analysis is a cornerstone of engineering design, ensuring that structures can withstand applied loads without failure or excessive deformation (Yang *et al*. 2023, Aktarer *et al*. 2025). It plays a critical role in predicting the behavior of structures under various loading conditions, including static, dynamic, and environmental forces (Ehyaei *et al*. 2016). Understanding stability is essential to prevent catastrophic failure, such as buckling in columns, collapse in bridges, or overturning in buildings (Salari *et al*. 2019). This analysis helps engineers design safer, more reliable structures that can maintain integrity over their expected lifespan (Salari *et al*. 2019). Stability analysis not only protects the safety of occupants but also minimizes the risks and costs associated with structural failure, reducing the need for repairs and maintenance (Zerrouki *et al*. 2020). It is particularly important in the design of slender or lightweight structures, where stability is more susceptible to subtle changes in load or geometry (Akbari *et al*. 2023). The complexity of modern engineering designs, especially with irregular geometries and composite materials, requires advanced stability analysis techniques to account for all variables (Babaei *et al*. 2021). In addition, stability analysis is essential in seismic, wind, and thermal load assessments, ensuring that structures can resist forces that may be unpredictable in magnitude or direction (Chen *et al*. 2019). Incorporating stability considerations into design also aids in optimizing materials, leading to more efficient, cost-effective construction methods (Avey *et al*. 2023). As engineering challenges evolve with increasing environmental pressures and technological advancements, stability analysis remains integral to creating resilient, high-performance systems (Safarpour *et al*. 2017, Zare *et al*. 2020).

In this study, the structural performance of concrete skew panels is enhanced using nanocomposite reinforcement, specifically focusing on FG-GOPRC materials. The reinforcement strategy aims to address common challenges associated with the structural integrity of skew panels under complex load conditions. A comprehensive analysis is conducted using the Halpin-Tsai homogenization method, which characterizes the nanocomposite's effective mechanical properties based on the distribution and interaction of fibers and matrix. To model the behavior of the concrete skew panels, the FSDT is employed, incorporating a variational version of Hamilton's principle for deriving the governing equations of motion. This framework allows for an accurate representation of shear effects and the deformation behavior of skew panels. To solve these equations, the Chebyshev-type Ritz technique is utilized, providing a high degree of accuracy and computational efficiency for the analysis of deflection, stress distribution, and vibration response under both static and dynamic loading. The results demonstrate that the use of FG-GOPRC nanocomposites significantly improves the bending stiffness, load-bearing capacity, and dynamic response of skew panels when compared to traditional concrete reinforcement techniques. The study provides insights into the optimal design and material selection for reinforced concrete panels in civil engineering applications, highlighting the role of nanocomposite materials in enhancing the durability and performance of structural components under various loading conditions. This research contributes to the ongoing development of advanced materials for sustainable infrastructure.

2. Problem formulation

The top view of the FG-GOPRC skew cylindrical concrete panel is shown in Fig. (1). It has an opening angle θ_o, a radius of curvature R, a curved edge of length b, and an oblique straight edge of length a, as shown in Fig. (1). Additionally, its planform has a skew angle α (with respect to the $\mathbb{y}$ axis), thus cylindrical panels with rectangular planforms are the particular case when $\alpha = 0$. The mathematical model is first developed in the orthogonal coordinate system $(\mathbb{x}, \mathbb{y}, \mathbb{z})$, and then it is transferred to the oblique coordinate system $(\hat{\mathbb{x}}, \hat{\mathbb{y}}, \mathbb{z})$ with the use of a rotation matrix. It should be mentioned that both coordinate systems have a parallel z axis and originate at the panel's mid-plane.

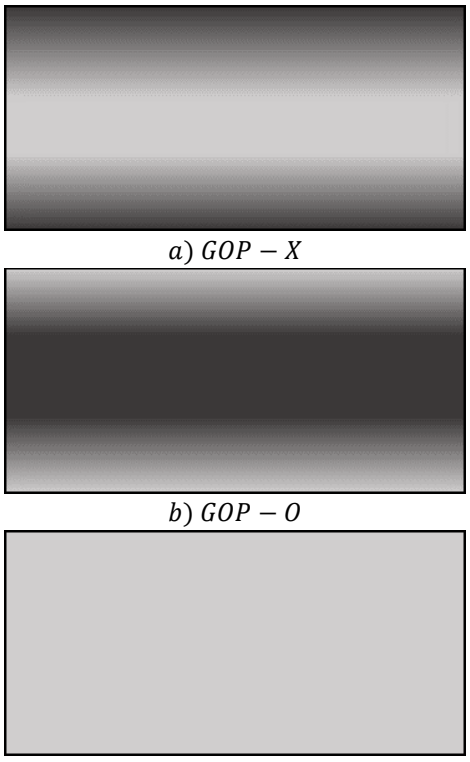

$a)\ GOP-X$

$b)\ GOP-O$

$c)\ GOP-UD$

Fig. 2 Along the thickness direction of the shell, there are three different patterns of GOP distribution

Fig. 2 depicts the composite structure that has been described. It is believed that the GOPs reinforcement is distributed in two symmetric patterns, GOP-X and GOP-O, either uniformly (GOP-UD) or functionally graded across the thickness.

The material properties of the concrete matrix and GOPs reinforcement are listed in Table 1.

2.1 Effective material properties for nanocomposites

The material properties are ascertained by extending the Halpin-Tsai homogenization method. It is now possible to express the Young's modulus as (Zhang *et al*. 2020):

$$E = 0.49 \times \frac{1+\xi_L \eta_L V_{GOP}}{1-\eta_L V_{GOP}} \times E_m + 0.51 \times \frac{1+\xi_t \eta_t V_{GOP}}{1-\eta_t V_{GOP}} \times E_m \quad (1)$$

in which, $\xi_L = \xi_t = 2\frac{d_{GOP}}{h_{GOP}}$, $V^*_{GOP} = \frac{W_{GOP}}{W_{GOP}+\left(\frac{\rho_{GPL}}{\rho_M}\right)(1-W_{GOP})}$, $\eta_l = -\frac{1-\left(\frac{E_{GOP}}{E_M}\right)}{\xi_l+\left(\frac{E_{GOP}}{E_m}\right)}$, and $\eta_t = -\frac{1-\left(\frac{E_{GOP}}{E_M}\right)}{\xi_t+\left(\frac{E_{GOP}}{E_m}\right)}$.

The mass density and effective Poisson's ratio may be obtained by using the mixing method from

$$\rho = \rho_{GOP}V_{GOP} + \rho_m(1-V_{GOP}),\ v = \nu_{GOP}V_{GOP} + \nu_m(1-V_{GOP}) \quad (2)$$

Finally, along with the thickness direction, the following GOP distribution kinds may be offered:

$$GOP-X: V_{GOP}(k) = 4V^*_{GOP}\left|\frac{\mathbb{z}_k}{h}\right|, \quad (3a)$$

$$GOP-O: V_{GOP}(k) = 2V^*_{GOP}\left(1-2\left|\frac{\mathbb{z}_k}{h}\right|\right), \quad (3b)$$

$$GOP-UD: V_{GOP}(k) = V^*_{GOP}. \quad (3c)$$

Here, $\mathbb{z}_k = -\frac{h}{2} + \frac{(k-1)\times h}{N_L-1}$, and $k = 1,2,3,\ldots,N_L$.

3. Governing equations in variational form

The Chebyshev-type Ritz technique is a powerful numerical method widely used to approximate solutions to boundary value problems in engineering, physics, and applied mathematics (Jena *et al*. 2021). This method combines two key mathematical concepts: The Ritz method, which is a variational approach for solving differential equations, and Chebyshev polynomials, a class of orthogonal polynomials known for their superior approximation properties. By integrating these two techniques, the Chebyshev-type Ritz method provides a more efficient and accurate way to solve complex problems, particularly in structural mechanics and vibration analysis (Wang and Teng, 2019).

The Ritz method, developed by the Russian mathematician Walter Ritz, is a widely used technique for approximating solutions to boundary value problems, especially those involving partial differential equations (PDEs). In this method, the solution to a problem is approximated by a linear combination of trial functions that satisfy the problem's boundary conditions. The goal is to minimize the error between the exact solution and the trial solution by selecting appropriate trial functions and coefficients. The Ritz method transforms the original problem into a finite-dimensional problem, making it easier to solve numerically.

However, the success of the Ritz method largely depends on the choice of trial functions. For simple problems with standard boundary conditions, polynomial functions may suffice. But for more complex problems, such as those involving irregular geometries or variable material properties, simple polynomials often fail to provide an accurate approximation. This limitation motivates the need for more advanced trial functions that can better capture the nuances of the problem.

Chebyshev polynomials are a family of orthogonal polynomials that have numerous applications in numerical analysis. They are particularly useful because of their minimization of the maximum deviation—a property known as the Chebyshev equioscillation. This property makes Chebyshev polynomials highly efficient in approximating functions, especially in situations where the solution is difficult to represent with simple polynomial expansions. The Chebyshev nodes, which are the roots of Chebyshev polynomials, provide a non-uniform distribution of points that enhances the accuracy of polynomial approximations, particularly near the boundaries of the domain.

The Chebyshev-type Ritz technique merges the Ritz method with Chebyshev polynomials to create a more efficient and accurate method for solving boundary value problems. Instead of using simple polynomials as trial functions, the method uses Chebyshev polynomials. These polynomials are particularly effective because they provide rapid convergence for smooth functions, requiring fewer terms to achieve high accuracy compared to traditional polynomial expansions. The basic idea is to approximate the solution as a sum of Chebyshev polynomials, and then minimize the error by solving for the coefficients of these polynomials.

The process begins by selecting a set of Chebyshev polynomials over the domain of the problem. These polynomials are then substituted into the variational formulation of the problem, leading to a system of equations for the unknown coefficients. This system is solved numerically, yielding an approximate solution to the problem. The efficiency of the Chebyshev-type Ritz technique comes from the fact that Chebyshev polynomials handle singularities and irregularities in the solution more effectively than traditional polynomial expansions.

The Chebyshev-type Ritz technique has been successfully applied to a wide range of problems in structural mechanics, vibration analysis, and fluid dynamics, where exact solutions are often not feasible. It is particularly useful for analyzing structures like beams, plates, and shells, where complex boundary conditions or geometries are present. The method's high accuracy and computational efficiency make it a preferred choice for solving large-scale problems that would otherwise be intractable using traditional methods.

In summary, the Chebyshev-type Ritz technique offers a robust and efficient approach for approximating solutions to complex boundary value problems. By leveraging the strengths of both the Ritz method and Chebyshev polynomials, it provides a powerful tool for engineers and scientists working with challenging problems in various fields of study.

The following is a simplified variational version of Hamilton's principle when external surface and body forces are absent:

$$\delta \int_0^t (U - T) d\mathbb{t} = 0. \tag{4}$$

has the following mathematical description, where $\mathbb{t}$ is the time parameter and U and T are the strain and kinetic energy components, respectively.

$$U = \frac{1}{2}\iiint_V \sigma^{\mathrm{T}} \mathcal{E}\, dV, T = \frac{1}{2}\iiint_V \rho \dot{\mathfrak{u}}^{\mathrm{T}} \dot{\mathfrak{u}}\, dV \tag{5}$$

The stress, strain, and displacement vectors, denoted by σ, $\mathcal{E}$ and $\mathfrak{u}$ in Eq. (5), are specified in the next subsection. Additionally, the time derivative operator is shown by taking use of the top dot.

3.1 Displacement and Strain Field

According to FSDT, the displacement vector at any point through the thickness of the structure, which consists of a displacement vector $\mathbf{u^0}$ and a rotation vector $\mathbf{u^1}$ at the mid-plane, can be expressed as follows without losing generality:

$$\mathbf{u}(\mathbb{x}, \mathbb{y}, \mathbb{z}) = \mathbf{u^0}(\mathbb{x}, \mathbb{y}, \mathbb{z}) + \mathbb{z}\mathbf{u^1}(\mathbb{x}, \mathbb{y}, \mathbb{z}), \tag{6}$$

wherein:

$$\mathbf{u} = \begin{Bmatrix} \mathfrak{u} \\ \mathfrak{v} \\ \mathfrak{w} \end{Bmatrix}, \qquad \mathbf{u^0} = \begin{Bmatrix} \mathfrak{u}_0 \\ \mathfrak{v}_0 \\ \mathfrak{w}_0 \end{Bmatrix}, \qquad \mathbf{u^1} = \begin{Bmatrix} \phi_{\mathbb{x}} \\ \phi_{\mathbb{y}} \\ 0 \end{Bmatrix} \tag{7}$$

The letters $\mathfrak{u}$, $\mathfrak{v}$ and $\mathfrak{w}$ stand for displacement components via the $\mathbb{x}$, $\mathbb{y}$, and $\mathbb{z}$ axes, respectively. Additionally, components linked to mid-plane points are distinguished from those of random points by the subscript "0." Finally, $\phi_{\mathbb{x}}$ and $\phi_{\mathbb{y}}$ show the rotation of the cross section in the $\mathbb{yz}$ and $\mathbb{xz}$ planes. As a result, the in-plane strain vector based on the displacement field of the skew cylindrical panel can be written as follows:

$$\boldsymbol{\mathcal{E}}(\mathbb{z}) = \left\{\varepsilon_{\mathbb{xx}}, \varepsilon_{\mathbb{yy}}, \varepsilon_{\mathbb{xy}}\right\}^T = \boldsymbol{\mathcal{E}^0} + \mathbb{z}\boldsymbol{\mathcal{E}^1} \tag{8}$$

The following definitions apply to $\boldsymbol{\mathcal{E}^0}$ and $\boldsymbol{\mathcal{E}^1}$, which have been used as membrane and bending stresses, respectively:

$$\begin{aligned} \boldsymbol{\mathcal{E}^0} &= \left\{\varepsilon_{\mathbb{xx}0}, \varepsilon_{\mathbb{yy}0}, \gamma_{\mathbb{xy}0}\right\}^T \\ &= \left\{\mathfrak{u}_{0,\mathbb{x}}, \mathfrak{w}_0/R + \mathfrak{v}_{0,\mathbb{y}}, \mathfrak{v}_{0,\mathbb{x}} + \mathfrak{u}_{0,\mathbb{y}}\right\}^T, \end{aligned} \tag{9a}$$

$$\boldsymbol{\mathcal{E}^1} = \left\{\kappa_{\mathbb{xx}}, \kappa_{\mathbb{yy}}, \kappa_{\mathbb{xy}}\right\}^T = \left\{\phi_{\mathbb{x},\mathbb{x}}, \phi_{\mathbb{y},\mathbb{y}}, \phi_{\mathbb{y},\mathbb{x}} + \phi_{\mathbb{x},\mathbb{y}}\right\}^T. \tag{9b}$$

The spatial derivative operator is shown above with a smaller comma. Additionally, the transverse shear stresses may be obtained as follows:

$$\boldsymbol{\mathcal{E}^s} = \begin{Bmatrix} \phi_{\mathbb{x}} + \mathfrak{w}_{0,\mathbb{x}} \\ \phi_{\mathbb{y}} + \mathfrak{w}_{0,\mathbb{y}} \end{Bmatrix} \tag{10}$$

As a Hookean-type material, the stress-strain relation for the GOPRC panel may be expressed as follows, in accordance with the semi-plane-stress conditions controlling the issue ($\sigma_{\mathbb{zz}} = 0$):

$$\boldsymbol{\sigma}^{(\mathbb{k})} = \mathbf{C}^{(\mathbb{k})} \begin{Bmatrix} \boldsymbol{\mathcal{E}}(\mathbb{z}) \\ \boldsymbol{\mathcal{E}^s} \end{Bmatrix} \tag{11}$$

The material stiffness matrix $\mathbf{C}$ in the above image has the following elements:

$$\mathbf{C}^{(\mathbb{k})} = \begin{bmatrix} \mathcal{C}_{11}^{(\mathbb{k})} & \mathcal{C}_{12}^{(\mathbb{k})} & 0 & 0 & 0 \\ \mathcal{C}_{21}^{(\mathbb{k})} & \mathcal{C}_{22}^{(\mathbb{k})} & 0 & 0 & 0 \\ 0 & 0 & \mathcal{C}_{44}^{(\mathbb{k})} & 0 & 0 \\ 0 & 0 & 0 & \mathcal{C}_{55}^{(\mathbb{k})} & 0 \\ 0 & 0 & 0 & 0 & \mathcal{C}_{66}^{(\mathbb{k})} \end{bmatrix}, \tag{12a}$$

$$\boldsymbol{\sigma}^{(\mathbb{k})} = \left\{\sigma_{\mathbb{xx}}^{(\mathbb{k})}, \sigma_{\mathbb{yy}}^{(\mathbb{k})}, \sigma_{\mathbb{xy}}^{(\mathbb{k})}, \sigma_{\mathbb{xz}}^{(\mathbb{k})}, \sigma_{\mathbb{yz}}^{(\mathbb{k})}\right\}^T. \tag{12b}$$

Each GOPRC lamina's effective mechanical characteristics may be used to compute the stiffness matrix's components.

$$\mathcal{C}_{11}^{(\mathbb{k})} = \mathcal{C}_{22}^{(\mathbb{k})} = \frac{E^{(\mathbb{k})}}{1 - \nu^{(\mathbb{k})^2}}, \tag{13a}$$

$$\mathscr{b}_{12}^{(\Bbbk)} = \mathscr{b}_{21}^{(\Bbbk)} = \frac{\upsilon^{(\Bbbk)}E^{(\Bbbk)}}{1-\nu^{(\Bbbk)^2}}, \tag{13b}$$

$$\mathscr{b}_{44}^{(\Bbbk)} = \mathscr{b}_{55}^{(\Bbbk)} = \mathscr{b}_{66}^{(\Bbbk)} = \frac{E^{(\Bbbk)}}{2(1+\nu^{(\Bbbk)})}. \tag{13c}$$

Sketching a coordinate transformation using the following mapping from orthogonal to oblique coordinates may be necessary if boundary criteria are difficult to meet.

$$\hat{\mathbb{x}} = \mathbb{x} - \mathbb{y}\tan(\alpha), \tag{14a}$$

$$\hat{\mathbb{y}} = \mathbb{y}\sec(\alpha), \tag{14b}$$

$$\hat{\mathbb{z}} = \mathbb{z}. \tag{14c}$$

Rotations in base coordinates and transformed coordinates have the following relationship based on the above-planned mapping:

$$\mathscr{f}_{\mathbb{x}}(\mathbb{x},\mathbb{y},\mathbb{t}) = \cos(\alpha)\mathscr{f}_{\hat{\mathbb{x}}}(\hat{\mathbb{x}},\hat{\mathbb{y}},\mathbb{t}), \tag{15a}$$

$$\mathscr{f}_{\mathbb{y}}(\mathbb{x},\mathbb{y},\mathbb{t}) = -\sin(\alpha)\mathscr{f}_{\hat{\mathbb{x}}}(\hat{\mathbb{x}},\hat{\mathbb{y}},\mathbb{t}) + \mathscr{f}_{\hat{\mathbb{y}}}(\hat{\mathbb{x}},\hat{\mathbb{y}},\mathbb{t}). \tag{15b}$$

Additionally, the conversion of spatial derivations may be found as:

$$()_{,\mathbb{x}} = ()_{,\hat{\mathbb{x}}}, \tag{16a}$$

$$()_{,\mathbb{y}} = -\tan(\alpha)()_{,\hat{\mathbb{x}}} + \sec(\alpha)()_{,\hat{\mathbb{y}}}. \tag{16b}$$

According to the coordinate transformation mentioned above, the reformed strain components are:

$$\boldsymbol{\mathcal{E}^0} = \begin{Bmatrix} \mathfrak{u}_{0,\hat{\mathbb{x}}} \\ \sec(\alpha)\mathfrak{v}_{0,\hat{\mathbb{y}}} - \tan(\alpha)\mathfrak{v}_{0,\hat{\mathbb{x}}} + \mathfrak{w}_0/R \\ \sec(\alpha)\mathfrak{u}_{0,\hat{\mathbb{y}}} - \tan(\alpha)\mathfrak{u}_{0,\hat{\mathbb{x}}} + \mathfrak{v}_{0,\hat{\mathbb{x}}} \end{Bmatrix}, \tag{17a}$$

$$\boldsymbol{\mathcal{E}^1} = \begin{Bmatrix} \mathscr{f}_{\hat{\mathbb{x}},\hat{\mathbb{x}}} \\ \sec(\alpha)\mathscr{f}_{\hat{\mathbb{y}},\hat{\mathbb{y}}} + \sec(\alpha)\tan(\alpha)\mathscr{f}_{\hat{\mathbb{x}},\hat{\mathbb{x}}} \\ -\tan(\alpha)\mathscr{f}_{\hat{\mathbb{x}},\hat{\mathbb{y}}} - \tan(\alpha)\mathscr{f}_{\hat{\mathbb{y}},\hat{\mathbb{x}}} \\ \mathscr{f}_{\hat{\mathbb{y}},\hat{\mathbb{x}}} + \mathscr{f}_{\hat{\mathbb{x}},\hat{\mathbb{y}}} - 2\sin(\alpha)\mathscr{f}_{\hat{\mathbb{x}},\hat{\mathbb{x}}} \end{Bmatrix}, \tag{17b}$$

$$\boldsymbol{\mathcal{E}^s} = \begin{Bmatrix} \cos(\alpha)\mathscr{f}_{\hat{\mathbb{x}}} + \mathfrak{w}_{0,\hat{\mathbb{x}}} \\ \mathscr{f}_{\hat{\mathbb{y}}} - \sin(\alpha)\mathscr{f}_{\hat{\mathbb{x}}} + \sec(\alpha)\mathfrak{w}_{0,\hat{\mathbb{y}}} - \tan(\alpha)\mathfrak{w}_{0,\hat{\mathbb{x}}} \end{Bmatrix}. \tag{17c}$$

Lastly, by remembering Eqs. (4)–(7), using coordinate transformation, integrating over thickness, and classifying terms, the governing motion equation may be obtained in variational form. However, as our goal is to solve the equations using an energy-based method, these equations are not given here.

4. Solution procedure

The present study uses the Chebyshev-type Ritz technique to derive the matrix form of equations governing the free vibration of the FG-GOPRC skew cylindrical panel because it has demonstrated its effectiveness in solving solid mechanics problems. A double series of a product of two one-dimensional admissible shape functions that are built using Chebyshev polynomials is used to extend basic variables in line with the Chebyshev-Ritz method:

$$\begin{Bmatrix} \mathfrak{u}_0(\hat{\mathbb{x}},\hat{\mathbb{y}},\mathbb{t}) \\ \mathfrak{v}_0(\hat{\mathbb{x}},\hat{\mathbb{y}},\mathbb{t}) \\ \mathfrak{w}_0(\hat{\mathbb{x}},\hat{\mathbb{y}},\mathbb{t}) \\ \mathscr{f}_{\hat{\mathbb{x}}}(\hat{\mathbb{x}},\hat{\mathbb{y}},\mathbb{t}) \\ \mathscr{f}_{\hat{\mathbb{y}}}(\hat{\mathbb{x}},\hat{\mathbb{y}},\mathbb{t}) \end{Bmatrix} = \sum_{\mathbb{m}=1}^{\mathbb{N}_{\hat{\mathbb{x}}}} \sum_{\mathbb{mm}=1}^{\mathbb{N}_{\hat{\mathbb{y}}}} \mathcal{T}_{\mathbb{mm}}(\hat{\mathbb{y}})\mathcal{T}_{\mathbb{m}}(\hat{\mathbb{x}}) \begin{Bmatrix} \mathbb{U}_{\mathbb{mm}}(\mathbb{t}) \\ \mathbb{V}_{\mathbb{mm}}(\mathbb{t}) \\ \mathbb{W}_{\mathbb{mm}}(\mathbb{t}) \\ \mathbb{X}_{\mathbb{mm}}(\mathbb{t}) \\ \mathbb{Y}_{\mathbb{mm}}(\mathbb{t}) \end{Bmatrix} \tag{18}$$

In addition to $\mathcal{T}_{\mathbb{m}}(\hat{\mathbb{x}})$ and $\mathcal{T}_{\mathbb{mm}}(\hat{\mathbb{y}})$, which are admissible shape functions and, as explained below, include $\mathbb{m}$-th and $\mathbb{mm}$-th order Chebyshev polynomials ($\mathbb{f}^{\mathfrak{D}}(\hat{\mathbb{x}}), \mathbb{g}^{\mathfrak{D}}(\hat{\mathbb{y}})$) and boundary functions ($\mathbb{f}^{\mathfrak{D}}(\hat{\mathbb{x}}), \mathbb{g}^{\mathfrak{D}}(\hat{\mathbb{y}})$, $\mathbb{N}_{\hat{\mathbb{x}}}$ and $\mathbb{N}_{\hat{\mathbb{y}}}$ determine the number of shape functions employed

$$\mathcal{T}_{\mathbb{m}}(\hat{\mathbb{x}}) = \mathbb{f}^{\mathfrak{D}}(\hat{\mathbb{x}})\mathcal{F}_{\mathbb{m}}(\hat{\mathbb{x}}), \tag{19a}$$

$$\mathcal{T}_{\mathbb{mm}}(\hat{\mathbb{y}}) = \mathbb{g}^{\mathfrak{D}}(\hat{\mathbb{y}})\mathcal{F}_{\mathbb{mm}}(\hat{\mathbb{y}}), \tag{19b}$$

$$\mathfrak{D} = \mathfrak{u}_0, \mathfrak{v}_0, \mathfrak{w}_0, \mathscr{f}_{\hat{\mathbb{x}}}, \mathscr{f}_{\hat{\mathbb{y}}}. \tag{19c}$$

First-kind Chebyshev polynomials that work with the setup under examination are expressed as follows:

$$\mathcal{F}_{\mathbb{m}}(\hat{\mathbb{x}}) = \cos(\arccos\left(-1 + \frac{2\hat{\mathbb{x}}}{a}\right)(-1+\mathbb{m})), \tag{20a}$$

$$\mathcal{F}_{\mathbb{mm}}(\hat{\mathbb{y}}) = \cos(\arccos\left(-1 + \frac{2\hat{\mathbb{y}}}{b}\right)(-1+\mathbb{mm})). \tag{20b}$$

The following form for boundary functions is utilized to make managing boundary conditions easier since multiple sets of boundary conditions are taken into consideration in this research.

$$\mathbb{f}^{\mathfrak{D}}(\hat{\mathbb{x}}) = \left(-\frac{\hat{\mathbb{x}}}{a} + 1\right)^{\hbar_2^{\mathfrak{D}}} \left(\frac{\hat{\mathbb{x}}}{a}\right)^{\hbar_1^{\mathfrak{D}}}, \tag{21a}$$

$$\mathbb{g}^{\mathfrak{D}}(\hat{\mathbb{y}}) = (-\frac{\hat{\mathbb{y}}}{b} + 1)^{\hbar_4^{\mathfrak{D}}} (\frac{\hat{\mathbb{y}}}{b})^{\hbar_3^{\mathfrak{D}}}, \tag{21b}$$

$$\mathfrak{D} = \mathfrak{u}_0, \mathfrak{v}_0, \mathfrak{w}_0, \mathscr{f}_{\hat{\mathbb{x}}}, \mathscr{f}_{\hat{\mathbb{y}}}. \tag{21c}$$

The current research may use a variety of boundary conditions. Boundary conditions are specified for clamped (C), free (F), hard simply supported (S*), and soft simply supported (S). Shape function adoption in the Ritz approach is known to be dependent solely on the fundamental kind of boundary condition. As a result, each of the specified boundary conditions requires the necessary kind of constraints. Table (2) contains a list of the restrictions.

Finally, by assigning the proper value to the $\hbar_i^{\mathfrak{D}}(i = 1,2,3,4)$, acceptable admissible functions may be generated. As previously stated, a variety of boundary conditions are used in this study.

The equations with spatial zeroth order derivatives and temporal second order derivatives are produced by recalling the definition of the Hamilton principle and adding the estimated displacement field. These equations may be expressed in matrix form as follows

$$\boldsymbol{\mathcal{M}}\ddot{\boldsymbol{\mathcal{S}}} + \boldsymbol{\mathcal{K}}\boldsymbol{\mathcal{S}} = \mathbf{0}. \tag{22}$$

In this case, $\boldsymbol{\mathcal{M}}$ stands for the mass matrix and $\boldsymbol{\mathcal{K}}$ for the stiffness matrix. The unknown vector made up of $\mathbb{U}_{\mathbb{mm}}(\mathbb{t}), \mathbb{V}_{\mathbb{mm}}(\mathbb{t}), \mathbb{W}_{\mathbb{mm}}(\mathbb{t}), \mathbb{X}_{\mathbb{mm}}(\mathbb{t}), \mathbb{Y}_{\mathbb{mm}}(\mathbb{t})$ is represented

Table 2 Crucial limitations for every border condition that has been established

Boundary Condition	Conditions on $\hat{x} = a$ and $\hat{x} = 0$	Conditions on $\hat{y} = b$ and $\hat{y} = 0$
C	$v_0, u_0, \not{f}_{\hat{x}}, w_0, \not{f}_{\hat{y}} = 0$	$v_0, u_0, \not{f}_{\hat{x}}, w_0, \not{f}_{\hat{y}} = 0$
S*	$u_0, w_0, v_0, \not{f}_{\hat{y}} = 0$	$u_0, w_0, v_0, \not{f}_{\hat{x}} = 0$
S	$v_0, \not{f}_{\hat{y}}, w_0 = 0$	$u_0, \not{f}_{\hat{x}}, w_0 = 0$
F	-	-

Table 3 The first three frequency characteristics of an isotropic skew cylindrical panel with $\alpha = \theta_0 = 30^o, a/R = 0.5, h/R = 0.01$

	$\breve{\Omega}_1$	$\breve{\Omega}_2$	$\breve{\Omega}_3$
Present	0.4204	0.4340	0.7396
Ref. (Kandasamy and Singh 2006)	0.421	0.434	0.736

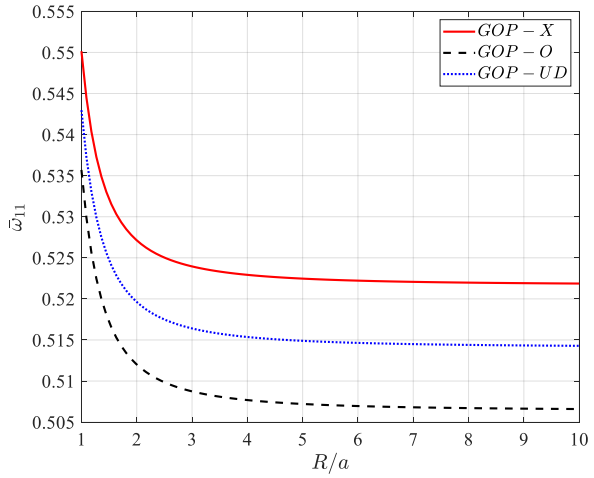

Fig. 3 The frequency characteristic of an isotropic skew cylindrical panel as a function of the radius-to-panel radius ratio

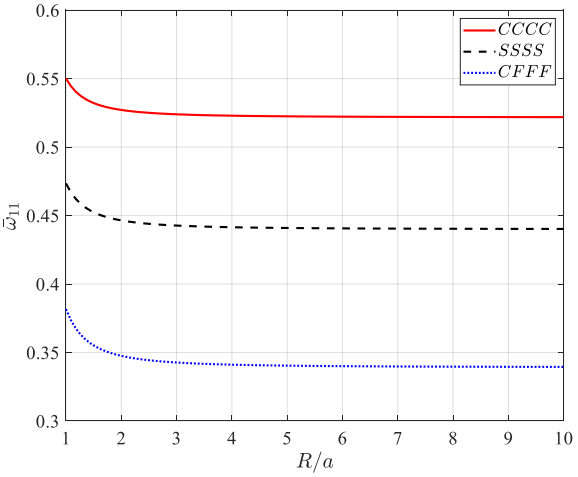

Fig. 4 The vibrational characteristic of an isotropic skew cylindrical panel subjected to various boundary conditions

by the meantime $\boldsymbol{\mathcal{S}}$. Finally, an eigenvalue-type equation in matrix form can be derived by substituting the previous equation with the general solution form for free vibrations, which is $\boldsymbol{\mathcal{S}} = \boldsymbol{s}e^{i\omega\mathbb{t}}$.

$$(\boldsymbol{\mathcal{K}} - \omega^2\boldsymbol{\mathcal{M}})\boldsymbol{s} = \mathbf{0}. \tag{23}$$

On the other hand, the non-trivial solution of Eq. (23) gives ω, which represents the system's free vibration frequency. Since dimensionless parameters are often more convenient to work with, the non-dimensional frequency parameter is introduced as $\Omega = \omega a\sqrt{\rho_m/E_m}$, and will be used from this point onward.

5. Result and discussion

5.1 Validation

Table 3 compares the first three frequency characteristics of an isotropic skew cylindrical panel subjected to different reinforcement configurations. Specifically, it compares the results obtained in the current study with those from Kandasamy and Singh (Kandasamy and Singh, 2006). The key parameters for the panel are a skew angle $\alpha = 30^o$, radius-to-radius ratio $a/R = 0.5$, and height-to-radius ratio $h/R = 0.01$. The frequency values for the present study are $\breve{\Omega}_1$=0.4204, $\breve{\Omega}_2$=0.4340, and $\breve{\Omega}_3$=0.7396. These values are in close agreement with the results from Kandasamy and Singh, where the frequencies were reported as $\breve{\Omega}_1$=0.421, $\breve{\Omega}_2$=0.434, and $\breve{\Omega}_3$ =0.736. The table thus serves to validate the effectiveness of the proposed reinforcement method in predicting the dynamic behavior of the skew cylindrical panels. By presenting the first three frequencies, this table provides important data for understanding the vibrational modes of the panel, which is vital for engineering applications involving concrete structures. The close match in frequency values also supports the accuracy and reliability of the numerical methods used in this study.

5.2. Parametric study

Fig. 3 presents a plot showing the frequency characteristic of an isotropic skew cylindrical panel as a function of the radius-to-panel radius ratio. The graph compares the vibrational frequencies for three different reinforcement configurations of functionally graded graphene oxide (GOP) within the panel: GOP-X, GOP-O, and GOP-UD. The x-axis represents the ratio, while the y-axis shows the frequency. The red curve, representing GOP-X, shows a relatively high initial frequency that decreases as the R/a ratio increases. The dashed black line represents GOP-O, which follows a similar trend, but with slightly lower frequencies compared to GOP-X. The blue dotted line corresponds to GOP-UD, which also shows a reduction in frequency as the R/a ratio increases, although it follows a slightly different slope compared to the other two reinforcement configurations. The behavior observed indicates that the reinforcement pattern significantly affects the vibrational characteristics of the skew panel, with GOP-X generally resulting in higher frequencies compared to GOP-O and GOP-UD. This plot provides valuable insight into how different reinforcement configurations influence

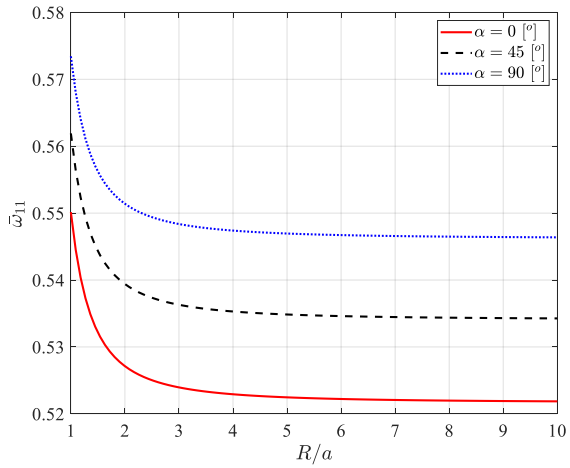

Fig. 5 The relationship between the skew angle and the natural frequency of skew concrete panels

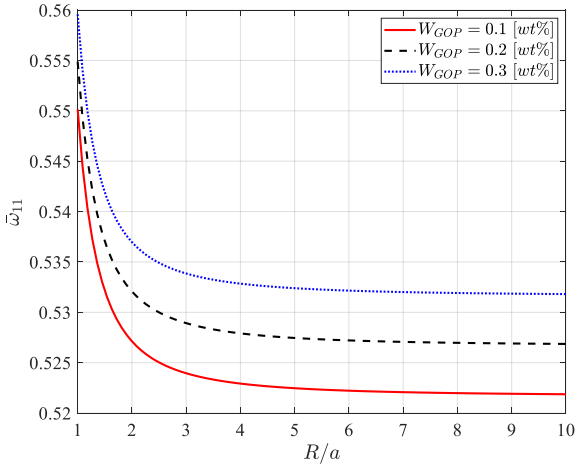

Fig. 6 The effect of the weight fraction of graphene oxide reinforcement on the natural frequency of skew concrete panels

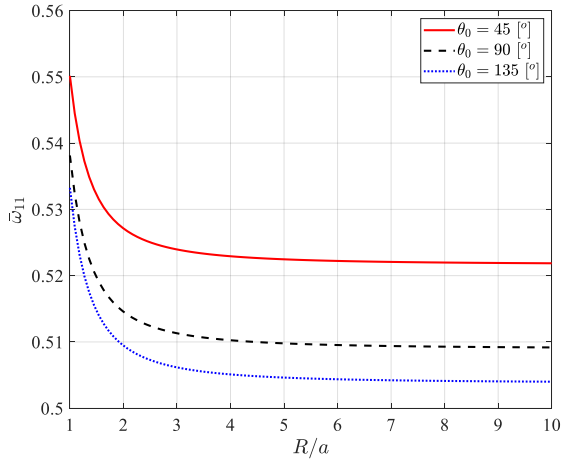

Fig. 7 The influence of the opening angle on the natural frequency of skew concrete panels

the vibrational response of the skew cylindrical panels, which is crucial for optimizing the panel's design for structural applications.

Fig. 4 displays a plot illustrating the vibrational characteristic of an isotropic skew cylindrical panel subjected to various boundary conditions. The graph compares the frequency behavior for three different support conditions: CCCC (Clamped), SSSS (Simply Supported), and CFFF (Clamped-Free-Free). The x-axis represents the radius-to-panel radius ratio, while the y-axis shows the frequency. The solid red line represents CCCC, which maintains the highest frequency across all R/a ratios. This indicates that clamped boundary conditions lead to the highest stiffness and the lowest deformation, resulting in higher frequencies. The dashed black line represents SSSS, which shows a noticeable decrease in frequency compared to CCCC. The dotted blue line corresponds to CFFF, which exhibits the lowest frequency, as expected from the free boundary conditions that allow for more deformation and lower stiffness. This figure underscores the significant effect that boundary conditions have on the vibrational properties of skew cylindrical panels. The results clearly indicate that clamped boundary conditions provide the highest structural integrity, while free or simply supported boundary conditions result in reduced frequencies and increased susceptibility to deformation. This analysis is crucial for understanding the behavior of panels under different real-world structural constraints.

Fig. 5 presents the relationship between the skew angle and the natural frequency of skew concrete panels. The plot analyzes three distinct skew angles: $\alpha = 0°$, $\alpha = 45°$, and $\alpha = 90°$. The x-axis represents the radius-to-thickness ratio, and the y-axis corresponds to the natural frequency of the panel. The results indicate that the natural frequency decreases with an increase in the skew angle. Specifically, non-skewed panels (with $\alpha = 0°$) exhibit the highest natural frequency, suggesting that the panel's stiffness is highest when it is not skewed. The frequency decreases progressively as the skew angle increases, with the $\alpha = 90°$ panels showing the lowest natural frequency. This trend reflects the influence of the geometric irregularity introduced by the skew angle, which compromises the structural stiffness of the panel. The decrease in frequency suggests a higher susceptibility to vibrational deformations, indicating that the skew angle has a substantial impact on the panel's dynamic behavior, influencing its overall performance in both static and dynamic loading conditions.

Fig. 6 investigates the effect of the weight fraction of graphene oxide reinforcement on the natural frequency of skew concrete panels. The x-axis represents the radius-to-thickness ratio, while the y-axis shows the natural frequency of the panel. The data reveal a clear trend: as the weight fraction of graphene oxide increases, the natural frequency also increases. This indicates that increasing the volume of nanocomposite reinforcement enhances the stiffness of the concrete skew panels, which in turn leads to higher natural frequencies. The higher reinforcement levels contribute to improved structural integrity and vibration resistance, suggesting that graphene oxide can significantly influence the dynamic properties of concrete panels. The findings highlight the importance of the reinforcement content in optimizing the structural performance of skew concrete panels, offering a potential approach for improving

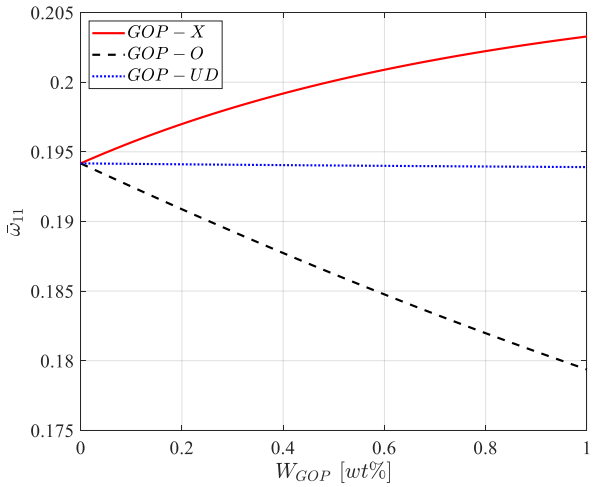

Fig. 8 The effect of different reinforcement patterns of graphene oxide on the natural frequency of skew concrete panels, as a function of the weight fraction of graphene oxide reinforcement

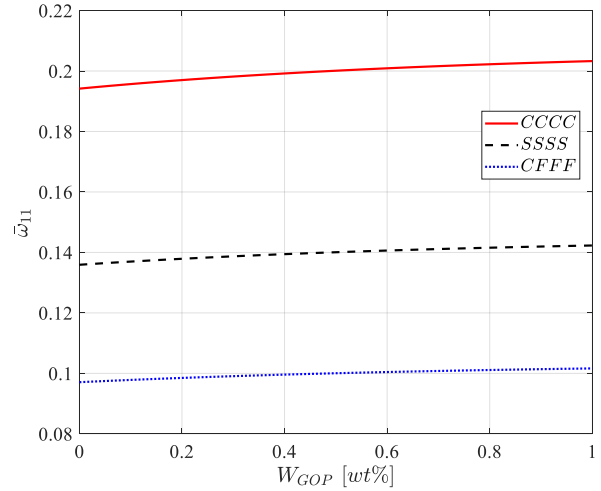

Fig. 9 The influence of different boundary conditions on the natural frequency of skew concrete panels

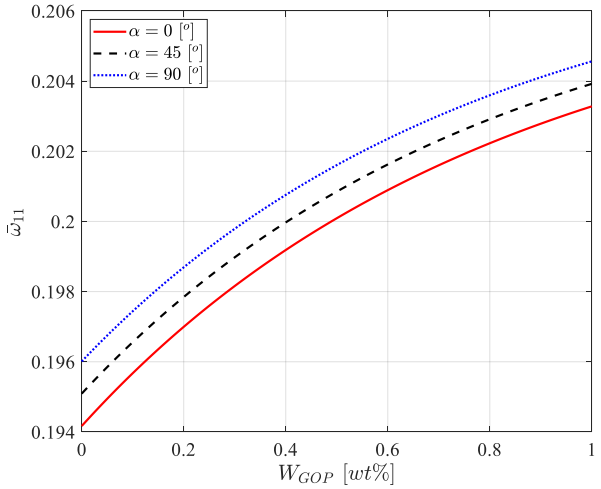

Fig. 10 The effect of the skew angle on the natural frequency of skew concrete panels, considering different graphene oxide reinforcement fractions

the load-bearing capacity and vibrational response of these panels under various dynamic and static loading conditions.

Fig. 7 explores the influence of the opening angle on the natural frequency of skew concrete panels. In this figure, the x-axis represents the radius-to-thickness ratio, and the y-axis displays the natural frequency of the panels. The results suggest that the natural frequency decreases with an increase in the opening angle. As the opening angle increases from 45° to 135°, the panels exhibit lower natural frequencies, indicating that larger opening angles result in a decrease in stiffness. This trend suggests that an increase in the gap or the geometric flexibility of the panel reduces its ability to resist vibrational deformations. The decreased natural frequency with a larger opening angle reflects the alteration of boundary conditions and the change in structural rigidity, which are critical factors in the panel's dynamic performance. This figure highlights the significance of geometric factors, such as the opening angle, in influencing the vibrational behavior and overall structural performance of skew concrete panels.

Fig. 8 investigates the effect of different reinforcement patterns of graphene oxide on the natural frequency of skew concrete panels, as a function of the weight fraction of graphene oxide reinforcement. The study compares three reinforcement patterns: GOP-X, GOP-UD, and GOP-O. The x-axis represents the weight fraction of graphene oxide, while the y-axis shows the natural frequency of the panels. The data demonstrates that, as the weight fraction increases, the natural frequency increases for all three reinforcement patterns. Notably, the GOP-X pattern shows the highest increase in natural frequency, followed by GOP-O and GOP-UD. This suggests that the distribution and arrangement of graphene oxide particles within the composite play a crucial role in determining the vibrational properties of the skew panels. The GOP-X pattern, which likely represents an optimized configuration, results in the most significant improvement in panel stiffness, providing enhanced resistance to vibrational deformation. These results underscore the importance of reinforcement pattern selection, indicating that functionally graded graphene oxide can be tailored to achieve desirable dynamic performance characteristics, thus improving the load-bearing capacity and stability of concrete skew panels under varying loading conditions.

Fig. 9 explores the influence of different boundary conditions on the natural frequency of skew concrete panels. The x-axis represents the weight fraction of graphene oxide reinforcement, ranging from 0 to 1 (0% to 100%), and the y-axis shows the natural frequency of the panel. Three boundary conditions are considered: CCCC (clamped-clamped), SSSS (simply supported), and CFFF (clamped-free). The results reveal that the CCCC boundary condition produces the highest natural frequency across all weight fractions of graphene oxide, with the frequency increasing as the graphene oxide content rises. In contrast, the SSSS and CFFF boundary conditions exhibit lower natural frequencies, particularly under lower reinforcement fractions. This suggests that the boundary conditions significantly influence the stiffness and vibrational behavior of the panels. The CCCC configuration, where both edges are

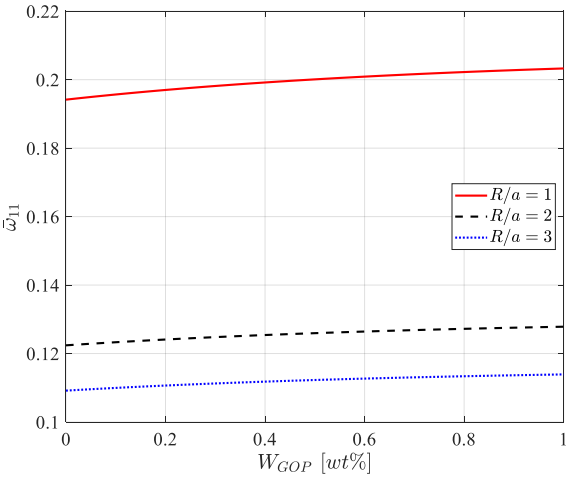

Fig. 11 The impact of the radius-to-thickness ratio on the natural frequency of skew concrete panels with varying graphene oxide reinforcement fractions

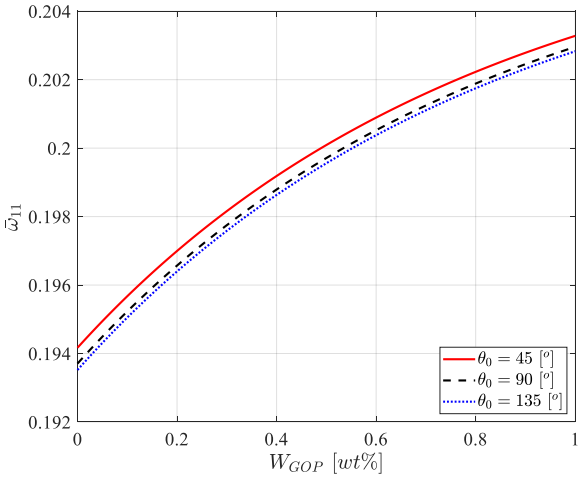

Fig. 12 The effect of the opening angle and GOP weight fraction on the natural frequency

clamped, restricts the panel's displacement more than the other boundary conditions, leading to higher frequencies. Conversely, the CFFF condition allows greater displacement at the free end, resulting in a lower natural frequency. These findings highlight the importance of boundary conditions in determining the dynamic performance of concrete skew panels reinforced with graphene oxide.

Fig. 10 investigates the effect of the skew angle on the natural frequency of skew concrete panels, considering different graphene oxide reinforcement fractions. The x-axis represents the weight fraction of graphene oxide, and the y-axis shows the natural frequency of the panel. The results indicate that, as the skew angle increases, the natural frequency increases for all levels of graphene oxide reinforcement. At higher skew angles, the panels show higher natural frequencies, suggesting that skewed panels with higher graphene oxide content become stiffer. The increasing natural frequency with both skew angle and reinforcement weight fraction indicates that higher graphene oxide reinforcement and skew angle both contribute to enhancing the structural integrity and vibrational resistance of the panels. The results emphasize the importance of considering both geometric factors (such as skew angle) and reinforcement content to optimize the dynamic performance of reinforced concrete skew panels.

Fig. 11 examines the impact of the radius-to-thickness ratio on the natural frequency of skew concrete panels with varying graphene oxide reinforcement fractions. The x-axis represents the weight fraction of graphene oxide, while the y-axis corresponds to the natural frequency of the panel. The results show that as the radius-to-thickness ratio increases, the natural frequency decreases. This trend is consistent across all levels of graphene oxide reinforcement. Panels with a higher radius-to-thickness ratio exhibit lower natural frequencies, indicating reduced stiffness. This behavior is likely due to the increased flexibility of panels with larger radii, making them more susceptible to vibrational deformations. Conversely, panels with smaller radius-to-thickness ratios exhibit higher natural frequencies, reflecting their increased stiffness and resistance to deformation. The data highlights the significant influence of geometric factors, such as the radius-to-thickness ratio, on the vibrational behavior of skew concrete panels and their dynamic performance when reinforced with graphene oxide.

Fig. 12 explores the effect of the opening angle and GOP weight fraction on the natural frequency of skew concrete panels. The x-axis represents the weight fraction of graphene oxide, and the y-axis shows the natural frequency of the panel. The results show that the natural frequency increases as the graphene oxide reinforcement fraction increases. Moreover, for higher opening angles, the natural frequency tends to be higher. The plot suggests that a larger opening angle leads to increased panel stiffness, which results in higher natural frequencies. As the graphene oxide content increases, the stiffness of the panel improves further, amplifying the effect of the opening angle on the dynamic behavior. These findings highlight the complex interaction between geometric factors such as the opening angle and material properties like the reinforcement fraction, underlining the importance of both in enhancing the vibrational performance and structural integrity of skew concrete panels reinforced with graphene oxide.

6. Conclusions

This study has successfully demonstrated the potential of FG-GOPRC nanocomposite materials in enhancing the structural integrity of concrete skew panels. The utilization of nanocomposite reinforcement in the concrete matrix was shown to provide significant improvements in mechanical properties, including bending stiffness, load-bearing capacity, and dynamic performance under both static and dynamic loading conditions. Through the integration of the Halpin-Tsai homogenization method, a precise characterization of the nanocomposite's effective material properties was achieved, accounting for the fiber distribution and interaction within the matrix. This methodology allowed for an in-depth analysis of the

material's behavior, ensuring a realistic and reliable prediction of the overall performance of the reinforced panels. The application of the FSDT along with a variational version of Hamilton's principle provided a robust framework for deriving the governing equations of motion for the skew panels. This approach accurately captures the shear effects and deformation behavior that are critical in the analysis of non-prismatic and irregularly shaped structural elements. The Chebyshev-type Ritz technique was employed to efficiently solve these equations, offering a balance between computational efficiency and the accuracy required for complex structural analysis. The results from this method revealed the enhanced performance of the reinforced skew panels, demonstrating that FG-GOPRC nanocomposites contribute to a marked reduction in deflection and an increase in the stability of the panels under applied loads. The findings of this research underscore the advantages of using advanced nanocomposite materials in the design of reinforced concrete structures. Specifically, the use of FG-GOPRC as a reinforcement material improves not only the mechanical properties of the skew panels but also their durability and resistance to failure. As infrastructure requirements continue to demand higher performance materials, this study provides valuable insights for the development and optimization of nanocomposite-enhanced concrete structures. Future work could focus on experimental validation and further exploration of the long-term effects of nanocomposite reinforcement in diverse structural applications. Ultimately, the proposed reinforcement methodology has the potential to lead to more sustainable, durable, and cost-effective concrete solutions in civil engineering.

Funding

Tertiary Education Scientific research project of Guangzhou Municipal Education Bureau (No. 2024312132) Guangzhou Municipal Science and Technology Bureau Basic and Applied Basic Research Project (No. SL2024 A04J01887).

Acknowledgment

The authors extend their appreciation to King Saud University, Saudi Arabia for funding this work through Ongoing Research Funding Program, (ORF-2025-704), King Saud University, Riyadh, Saudi Arabia.

References

Afolabi, O.A. and Ndou, N. (2024), "Synergy of hybrid fillers for emerging composite and nanocomposite materials—a review", *Polymers*, **16**(13), 1907. https://doi.org/10.3390/polym16131907

Akbari, M., Sadighi, M., Eslami, M. and Kiani, Y. (2023), "Axisymmetric free vibration analysis of functionally graded sandwich annular plates: a quasi-3d shear and normal deformable model", *Int. J. Struct. Stabil. Dyn.*, **23**(8), 2350086. https://doi.org/10.1142/S0219455423500864

Aktarer, S.M., Kucukomeroglu, T., Sekban, D.M., Yaylaci, E.U., Yaylaci, M., Ozdemir, M.E. and Mirzaloglu, I. (2025), "Analysis of the changes in microstructure, mechanical, and contact properties of multi-pass friction stir processed dp800 steel", *Adv. Nano Res.*, **18**(3), 253-264. https://doi.org/10.12989/anr.2025.18.3.253

Allahkarami, F. and Tohidi, H. (2021), "Size-dependent nonlinear free vibration of multilayer functionally graded graphene nanocomposite timoshenko microbeam under different boundary conditions", *Eur. Phys. J. Plus*, **137**(1), 5. https://doi.org/10.1140/epjp/s13360-021-02193-2

Anh, V. M., Quan, T. Q. and Tran, P. (2021), "Nonlinear vibration and geometric optimization of nanocomposite multilayer organic solar cell under wind loading", *Thin Walled Struct.*, **158**, 107199. https://doi.org/10.1016/j.tws.2020.107199

Arshid, E., Azimi, M., Moradi, M., Ouni, M.H.E. and Alashker, Y. (2025), "Mathematical solution for vibrational response of shear and normal deformable advanced metal foam cmbs treated with nanocomposite actuators", *Int. J. Struct. Stabil. Dyn.*, **25**(11), 2550118. https://doi.org/10.1142/S0219455425501184

Avey, M., Fantuzzi, N. and Sofiyev, A. (2023), "Thermoelastic stability of cnt patterned conical shells under thermal loading in the framework of shear deformation theory", *Mech. Adv. Mater. Struct.*, **30**(9), 1828-1841. https://doi.org/10.1080/15376494.2022.2045653

Babaei, H., Kiani, Y. and Reza Eslami, M. (2021), "Perturbation method for thermal post-buckling analysis of shear deformable fg-cntrc beams with different boundary conditions", *Int. J. Struct. Stabil. Dyn.*, **21**(13), 2150175. https://doi.org/10.1142/S0219455421501753

Babaei, H., Zavari, S., Kaveh, A., Arshid, E. and Civalek, Ö. (2024), "Dynamic response of advanced lightweight porous plates integrated with nanocomposite face sheets resting on elastic substrate", *Int. J. Struct. Stabil. Dyn.*, **25**(12), 2550132. https://doi.org/10.1142/S0219455425501329

Belabed, Z., Bousahla, A. A. and Tounsi, A. (2024), "Vibrational and elastic stability responses of functionally graded carbon nanotube reinforced nanocomposite beams via a new quasi-3d finite element model", *Comput. Concr.*, **34**(5), 625-648. https://doi.org/10.12989/cac.2024.34.5.625

Birenboim, M., Nadiv, R., Alatawna, A., Buzaglo, M., Schahar, G., Lee, J., Kim, G., Peled, A. and Regev, O. (2019), "Reinforcement and workability aspects of graphene-oxide-reinforced cement nanocomposites", *Compos. Part B Eng.*, **161**, 68-76. https://doi.org/10.1016/j.compositesb.2018.10.030

Chen, X., Lu, Y. and Li, Y. (2019), "Free vibration, buckling and dynamic stability of bi-directional fg microbeam with a variable length scale parameter embedded in elastic medium", *Appl. Math. Modell.*, **67**, 430-448. https://doi.org/10.1016/j.apm.2018.11.004

Ebrahimi, F. and Ezzati, H. (2024), "Dynamic analysis of thermally affected nanocomposite plates reinforced with functionalized graphene oxide nanoparticles", *Acta Mechanica*. **235**(1), 337-354. https://doi.org/10.1007/s00707-023-03754-5

Ehyaei, J., Ebrahimi, F. and Salari, E. (2016), "Nonlocal vibration analysis of fg nano beams with different boundary conditions", *Adv. Nano Res.*, **4**(2), 085. https://doi.org/10.12989/anr.2016.4.2.085

Gayatri, R., Yuliwati, E., Jaafar, J., Fizal, A.N.S., Hossain, M.S., Zulkifli, M., Yahaya, A.N.A. and Taweepreda, W. (2024), "Polymer-based nanocomposite membranes for industrial wastewater treatment: a review", *J. Environ. Chem. Eng.*, **12**(5), 113276. https://doi.org/10.1016/j.jece.2024.113276

Jena, S.K., Chakraverty, S. and Malikan, M. (2021), "Application of shifted chebyshev polynomial-based rayleigh-ritz method and

Navier's technique for vibration analysis of a functionally graded porous beam embedded in kerr foundation", *Eng. Comput.*, **37**, 3569-3589. https://doi.org/10.1007/s00366-020-01018-7

Kandasamy, S. and Singh, A.V. (2006), "Free vibration analysis of skewed open circular cylindrical shells", *J. Sound Vib.*, **290**(3-5), 1100-1118. https://doi.org/10.1016/j.jsv.2005.05.010

Li, J. and Liu, J. (2025), "Nonlinear optimized pid vibration control of thermal-dependent fg composite porous plates reinforced by agglomerated cnts", *Int. J. Struct. Stabil. Dyn.*, **25**(4), 2550034. https://doi.org/10.1142/S0219455425500348

Liu, L., Chang, D. and Gao, C. (2024), "A review of multi-functional nanocomposite fibers: design, preparation and applications", *Adv. Fiber Mater.*, **6**(1), 68-105. https://doi.org/10.1007/s42765-023-00340-1

Lu, S., Xue, N., Ma, W., Song, X. and Jiang, X. (2025), "Linear and nonlinear dynamics responses of an axially moving laminated composite plate-reinforced with graphene nanoplatelets", *Int. J. Struct. Stabil. Dyn.*, **25**(4), 2550036. https://doi.org/10.1142/S0219455425500361

Mamidi, N., Delgadillo, R.M., Sustaita, A.O., Lozano, K. and Yallapu, M.M. (2025), "Current nanocomposite advances for biomedical and environmental application diversity", *Med. Res. Rev.*, **45**(2), 576-628. https://doi.org/10.1002/med.22082

Rayhan, M.T., Islam, M.A., Khan, M., Hasan, M.A., Mobarak, M.H., Rimon, M.I.H. and Hossain, N. (2024), "Advances in additive manufacturing of nanocomposite materials fabrications and applications", *Eur. Polym. J.*, **220**, 113406. https://doi.org/10.1016/j.eurpolymj.2024.113406

Safarpour, H., Mohammadi, K. and Ghadiri, M. (2017), "Temperature-dependent vibration analysis of a fg viscoelastic cylindrical microshell under various thermal distribution via modified length scale parameter: a numerical solution", *J. Mech. Behav. Mater.*, **26**(1-2), 9-24. https://doi.org/10.1515/jmbm-2017-0010

Salari, E., Ashoori, A. and Vanini, S.A.S. (2019), "Porosity-dependent asymmetric thermal buckling of inhomogeneous annular nanoplates resting on elastic substrate", *Adv. Nano Res.*, **7**(1), 25. https://doi.org/10.12989/anr.2019.7.1.025

Tounsi, A., Belabed, Z., Bounouara, F., Balubaid, M., Mahmoud, S., Bousahla, A.A. and Tounsi, A. (2024), "A finite element approach for forced dynamical responses of porous fg nanocomposite beams resting on viscoelastic foundations", *Int. J. Struct. Stabil. Dyn.*, 2650078. https://doi.org/10.1142/S0219455426500781

Wang, Y.Q. and Teng, M.W. (2019), "Vibration analysis of circular and annular plates made of 3d graphene foams via chebyshev-ritz method", *Aerosp. Sci. Technol.*, **95**, 105440. https://doi.org/10.1016/j.ast.2019.105440

Yang, C., Su, C., Hu, H., Habibi, M., Safarpour, H. and Amine Khadimallah, M. (2023), "Performance optimization of photovoltaic and solar cells via a hybrid and efficient chimp algorithm", *Solar Energy*, **253**, 343-359. https://doi.org/10.1016/j.solener.2023.02.036

Zare, R., Najaafi, N., Habibi, M., Ebrahimi, F. and Safarpour, H. (2020), "Influence of imperfection on the smart control frequency characteristics of a cylindrical sensor-actuator gplrc cylindrical shell using a proportional-derivative smart controller", *Smart Struct. Syst.*, **26**(4), 469-480. https://doi.org/10.12989/sss.2020.26.4.469

Zerrouki, R., Karas, A. and Zidour, M. (2020), "Critical buckling analyses of nonlinear FG-CNT reinforced nano-composite beam", *Adv. Nano Res.*, **9**(3), 211-220. https://doi.org/10.12989/anr.2020.9.3.211

Zhang, Y., Li, J. and Abbas, M. (2024), "Dynamic stability analysis of CFRP sandwich structure reinforced by advanced nanocomposites via both machine learning method and mathematical simulation", *Mech. Adv. Mater. Struct.*, 1-24. https://doi.org/10.1080/15376494.2024.2329461

Zhang, Z., Li, Y., Wu, H., Zhang, H., Wu, H., Jiang, S. and Chai, G. (2020), "Mechanical analysis of functionally graded graphene oxide-reinforced composite beams based on the first-order shear deformation theory", *Mech. Adv. Mater. Struct.*, **27**(1), 3-11. https://doi.org/10.1080/15376494.2018.1444216

CC